

Flow-induced vibration and energy harvesting of an elastically mounted circular cylinder with mechanically coupled rotation

Ming Zhao D, Qin Zhang D and Yong Liu

Corresponding authors: Qin Zhang, zhangqin2000@ouc.edu.cn; Yong Liu, liuyong@ouc.edu.cn

(Received 11 May 2025; revised 10 July 2025; accepted 1 September 2025)

One-degree-of-freedom flow-induced vibration (FIV) and energy harvesting through FIV of an elastically mounted circular cylinder with mechanically coupled rotation were investigated numerically for low Reynolds number 100, mass ratio 8 and a wide range of reduced velocities. The aims of this study are to investigate the effect of the flow direction angle β on the vibration and energy harvesting through FIV. Two types of lock-in are found: vortex-induced vibration (VIV) and galloping. The response amplitude increases with the increase of β in both regimes. Both VIV response and galloping regimes are found for $\beta = 45^{\circ}$ to $\beta = 90^{\circ}$. For $\beta = -90^{\circ}$ to $\beta = 0^{\circ}$, only VIV response regimes are found. The fluid force and fluid torque play different roles in exciting/damping the vibration. In the high-amplitude gallop regime, the fluid force excites the vibration, and the torque damps the vibration. Energy harvesting at flow direction angle 90° is investigated as this flow direction has the maximum galloping amplitude. The energy harvesting is achieved by a linear electric damping coefficient in the numerical model. The maximum harvestable power in the galloping regime is significantly greater than that in the VIV regime, and it increases with the increase of the reduced velocity. When the reduced velocity is 20, the harvested power is over 20 times that in the VIV regime, and can further increase if reduced velocity further increases. The maximum efficiency over all simulated parameters is 0.424, occurring when the reduced velocity is 20, and electric damping factor is 0.04.

Key words: flow control, vortex shedding

¹School of Engineering, Design and Built Environment, Western Sydney University, Penrith, 2751, NSW, Australia

²School of Engineering, Ocean University of China, Qingdao, PR China

1. Introduction

Flow-induced vibration (FIV) has been studied extensively because it is a key mechanism that causes fatigue failure of structures in fluid flow. An elastically mounted rigid circular cylinder in a fluid flow has been used as the set-up for investigating fundamental mechanisms of FIV. Vortex-induced vibration (VIV) is the main format of FIV, and it occurs when there is synchronisation between the frequency of the wake vortex mode and the frequency of the vibration (Williamson & Govardhan 2004). The non-dimensional parameters that affect VIV of an elastically mounted circular cylinder are the reduced velocity defined as $U_r = U/(f_n D)$, mass ratio defined as $m^* = m/m_d$, and damping ratio $\zeta = C/(2\sqrt{km})$, where U is the free-stream velocity, f_n is the natural frequency of the system, D is the diameter of the cylinder, m is the mass of the cylinder, m_d is the displaced mass, c is the damping coefficient, and k is the stiffness. One-degree-of-freedom VIV of a cylinder in the crossflow direction has been the topic of many studies. Under low mass ratios, the lock-in regime of the reduced velocity is divided into three branches: initial branch, upper branch and lower branch (Khalak & Williamson 1996, 1999), and there is hysteresis near the boundaries between branches. Various types of effective passive and active flow control methods have been proposed to reduce VIV, and they have been reviewed by Hong & Shah (2018) and Zhao (2023). Active flow control needs to input energy into the system, and a passive flow control method reduced the VIV by attaching some devices on the cylinder, such as control rods, helical strakes, splitters and fins.

Studies have also been conducted to enhance VIV as FIV can be utilised as a source of renewable energy. Soti *et al.* (2017) developed a simple electromagnetic system for energy harvesting from VIV, while Yadav & Baredar (2018) summarised the studies of energy harvesting from VIV through piezoelectric systems. Taheri, Zhao & Wu (2023) and Chen, Li & Yang (2024) used rotating control rod and shape optimisation to enhance VIV, respectively. Taheri *et al.* (2023) reported that the vibration amplitude of the cylinder increases with the increase of the rotation speed of the control rod. However, the enhancement of the vibration is achieved at the cost of energy input that is used to rotate the rod. By optimising the shape of the cylinder, Chen *et al.* (2024) achieved more than a tenfold increase in the energy harvesting.

Nitti, De Cillis & De Tullio (2022) proposed a new concept of enhanced VIV through an elastically mounted cylinder with mechanically coupled rotation, as illustrated in figure 1(a) for reduced velocities up to 12. In the coupled system, the cylinder rolls along a straight rail with rotation radius r. The rail has inclination angle β relative to the flow direction in a fluid flow; β is 90° when the cylinder is on the upstream side of the rail, and -90° when the cylinder is on the downstream side. For a cylinder with finite length, the rolling of the cylinder can be achieved through a pair of linear guide rails with rack gear installed on the two ends of the cylinder, respectively. In Nitti *et al.* (2022), the configuration was treated as two-dimensional, and two-dimensional numerical simulations were conducted. They investigated the case where the vibration direction is perpendicular to the flow direction, i.e. the flow direction angle is $\beta = 90^{\circ}$. Nitti *et al.* (2022) found that up to the reduced velocity $V_r = 12$, the vibration amplitude increases with the increase of the reduced velocity, and the rotation radius r affects the response significantly.

Figure 1(b) is a sketch to demonstrate that the vibration amplitude will continue increasing as the reduced velocity further increases. In the figure, the cylinder is moving upwards with velocity \dot{X} during vibration in the case $\beta = 90^{\circ}$. The upward motion of the cylinder causes the rotation of the cylinder, with rotation speed $\dot{\theta} = \dot{X}/r$. The rotation of the cylinder in the clockwise direction causes an upward force F_X in the X-direction due to the Magnus effect (Prantl 1926; Swanson 1961). When the cylinder

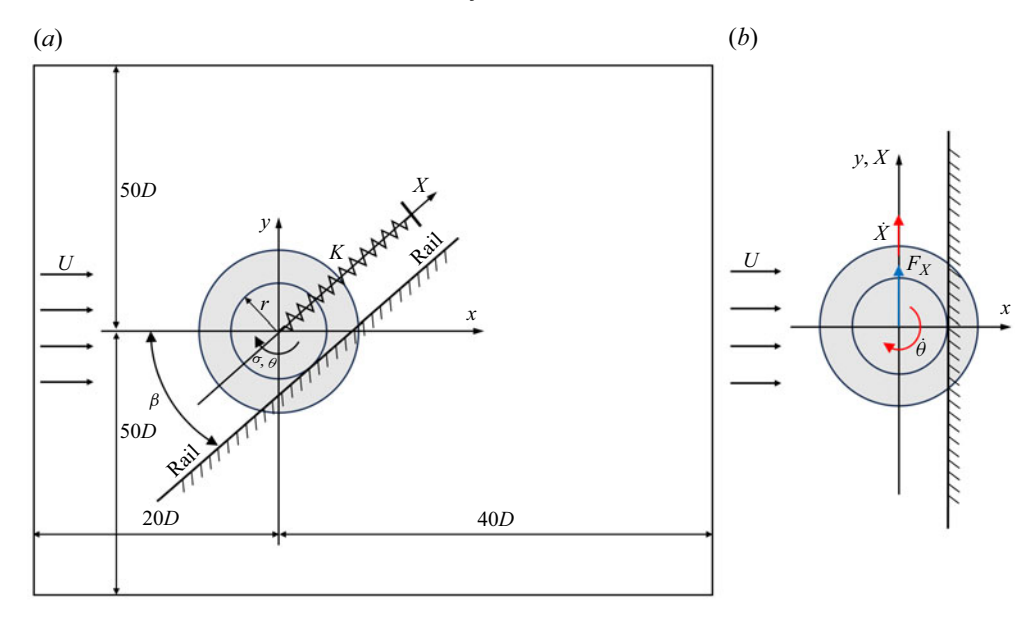


Figure 1. Computational domain for simulating vibration of a circular cylinder mechanically coupled with rotation using computational fluid dynamics. (a) Computational domain and (b) Velocity and force of the cylinder at $\beta = 90$.

moves downwards, the force due to the Magnus effect is also downwards. This force that is in the same direction as the velocity of the cylinder is equivalent to the negative damping of flow-induced galloping; as a result, the vibration amplitude increases with the increase of the reduced velocity. If the angle is $\beta = -90^{\circ}$, then the Magnus effect acts as positive damping because its force is in the direction opposite to the velocity of the cylinder. Nitti *et al.* (2022) predicted that the coupled rotation has potential to enhance energy harvesting.

In this paper, FIV and energy harvesting from FIV of a circular cylinder mechanically coupled with rotation placed in a uniform flow as shown figure 1 are investigated for flow directional angles (β) ranging from -90° to 90° . The spring-supported cylinder is allowed to vibrate translationally in the *X*-direction, which has inclination angle β relative to the income flow direction. The cylinder rolls along a straight line with rotation radius r. The angular displacement and angular speed of the cylinder's rolling are θ and σ , respectively. The vibration is a one-degree-of-freedom vibration because the cylinder translational displacement X and the angular displacement θ are related by $X = r\theta$. Nitti $et\ al.\ (2022)$ investigated the effects of the rotation radius r on the response for the case where the vibration direction is perpendicular to the flow direction, i.e. $\beta = 90^{\circ}$, and achieved significant increase in the vibration amplitude. In this study, the effect of the vibration direction angle β on the response will be investigated. The Reynolds number is Re = 100, and the mass ratio is $m^* = 8$. The Reynolds number is defined as Re = UD/v, where v is the kinematic viscosity of the fluid.

2. Numerical method

The dimensional equation of motion of the cylinder is (Nitti et al. 2022)

$$\left(m + \frac{I_0}{\hat{r}^2}\right) \frac{\mathrm{d}^2 \hat{X}}{\mathrm{d}\hat{r}^2} + C \frac{\mathrm{d}\hat{X}}{\mathrm{d}\hat{t}} + K \hat{X} = \hat{F}_e, \tag{2.1}$$

where variables with a hat are dimensional variables, \hat{X} is the displacement of the cylinder, m and I_0 are the mass and the polar mass moment of inertia of the cylinder, respectively, C is the translational damping coefficient in the X-direction, \hat{t} is time, \hat{F}_X is the fluid force in the X-direction, \hat{T}_{θ} is the fluid torque on the cylinder in the clockwise direction, $\hat{F}_e = \hat{F}_X + (\hat{T}_{\theta}/\hat{r})$ is referred to as equivalent force, and \hat{r} is the rotation radius of the cylinder. The cylinder is homogeneous, so the polar moment of inertia of the cylinder is $I_0 = \rho_c J_0$, where ρ_c is the density of the cylinder, and $J_0 = \pi D^4/32$ is the polar area moment of inertia. The mass ratio is $m^* = \rho_c/\rho$, where ρ is the density of the fluid. The natural frequency of the system is $f_n = (1/2\pi)\sqrt{K/(m+(I_0/\hat{r}^2))}$, and the reduced velocity is defined as $V_r = U/(f_n D)$.

The non-dimensional displacement (X), coordinates (x, y), time (t) and velocity vector (u, v) are defined as $X = \hat{X}/D$, $(x, y) = (\hat{x}, \hat{y})/D$, $t = U\hat{t}/D$ and $(u, v) = (\hat{u}, \hat{v})/U$, respectively. The non-dimensional form of (2.1) is

$$m^* e^{\frac{d^2 X}{dt^2}} + C^* \frac{dX}{dt} + K^* X = F^*,$$
 (2.2)

where $e = A_c/D^2 + J_0/(D^2\hat{r}^2)$, $C^* = C/(\rho DU)$, $K^* = K/(\rho U^2)$, $F^* = \hat{F}_X/(\rho DU^2) + \hat{T}_\theta/(\rho r D^2 U^2)$, and A_c is the cross-sectional area of the cylinder.

Figure 1(a) shows the rectangular computational domain with non-dimensional length 60 in the flow direction and height 100 in the crossflow direction for simulating the fluid flow past the vibrating cylinder. The neutral position of the cylinder is located at 20 downstream from the inlet boundary. To account for the continuously moving boundary caused by the vibration, the Navier–Stokes (NS) equations are solved using the arbitrary Lagrangian–Eulerian (ALE) scheme that allows the mesh to deform. The non-dimensional incompressible NS equations in the ALE scheme are

$$\frac{\partial u_i}{\partial t} + \left(u_j - u_{j,m}\right) \frac{\partial u_i}{\partial x_i} + \frac{\partial p}{\partial x_i} = \frac{1}{Re} \frac{\partial^2 u_i}{\partial x_i x_i},\tag{2.3}$$

$$\frac{\partial u_i}{\partial x_i} = 0, (2.4)$$

where subscript i=1, 2 on a vector represents the components in the x- and y-directions, respectively, the non-dimensional pressure is $p=p/\rho U^2$, and $u_{j,m}$ is the velocity of the computational mesh in the x_i -direction.

The NS equations are solved using the Petrov–Galerkin finite element method and inhouse CFD software developed by Zhao *et al.* (2007), which has been successfully used in studies of VIV or rotating and non-rotating cylinders (Zhao 2013, 2020; Munir *et al.* 2021; Taheri *et al.* 2023). The boundary conditions are specified as follows. On the inlet, non-dimensional flow velocity is 1, and the pressure gradient in the streamwise direction is zero. On the outlet, the reference pressure is zero, and the gradient of the velocity in the streamwise direction is zero. On the surface of the cylinder, a no-slip boundary condition is given, i.e. the fluid velocity is the same as the velocity of the cylinder surface. On the two side boundaries, symmetric boundary conditions are used. The initial condition for all the simulations is that the velocity is zero in the whole computational domain. The initial condition may affect the response near the boundary between response branches where the vibration is hysteretic (Prasanth & Mittal 2008). This paper is focused on identifying response modes; identifying the effects of initial condition on vibration is not covered.

In the ALE scheme, the computational mesh is deformed to account for the updated position of the cylinder in every computational time step. The equation for calculation of

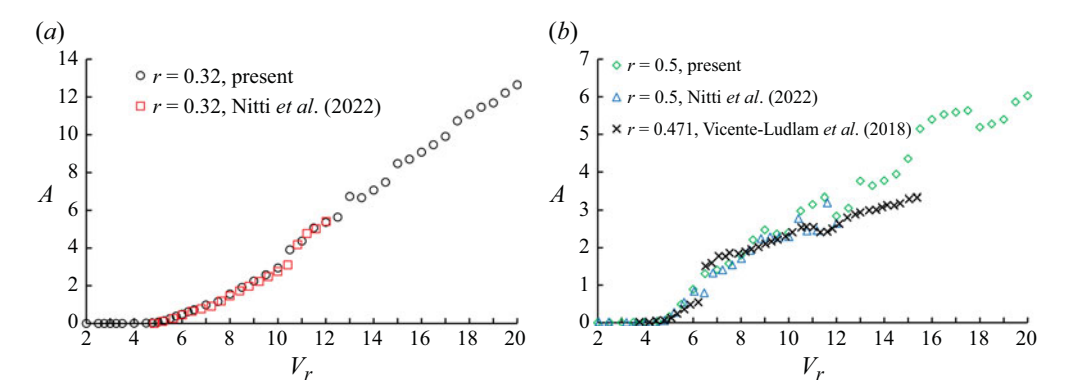


Figure 2. Comparison between the present numerical results and other numerical and experimental results at $\beta = 90^{\circ}$: (a) r = 0.32, (b) r = 0.5.

the displacement of the finite element nodes is (Zhao & Cheng 2011)

$$\nabla \cdot (\gamma \nabla S_i) = 0, \tag{2.5}$$

where S_i is displacement of the mesh nodes in the x_i -direction, and γ is a parameter that controls the deformation of the mesh. A refined mesh is used near the cylinder surface to ensure that the flow separation is well predicted. To ensure that mesh near the cylinder has smaller deformation, the parameter γ in a finite element is chosen as $\gamma = 1/A_e$, where A_e is the area of the finite element. When (2.5) is solved by the finite element method, the following boundary conditions are specified. On the inlet and outlet boundaries (the left-and right-hand boundaries in figure 1a), $S_1 = 0$ and $\partial S_2/\partial x = 0$. On the top and bottom boundaries, $S_2 = 0$ and $\partial S_1/\partial x = 0$. On the surface of the cylinder, the displacement of the mesh nodes is the same as the displacement of the cylinder. The boundary conditions allow the mesh nodes to slide on the four side boundaries.

In each computational time step, the NS equations are first solved, and the fluid force and torque on the cylinder are obtained based on the fluid pressure and shear stress on the cylinder surface. Then the equation of motion (2.2) is solved to obtain the cylinder's displacement and velocity. Finally, (2.5) is solved to calculate the updated displacement of the mesh nodes, and find the mesh velocity u_{jm} , which is required for solving the NS equations using ALE.

3. Validation and mesh dependency test

The validity of the present numerical method for the case of a circular cylinder without mechanically coupled rotation has been proved in our previous studies (Zhao 2013). To further validate the numerical method for a cylinder coupled with rotation, figure 2 shows a comparison between the present numerical results for $m^* = 8$ and Nitti *et al.* (2022), where the vibration amplitude A is defined as $A = (X_{max} - X_{min})/2$, with X_{max} and X_{min} the maximum and minimum vibration displacements, respectively. Good agreement between the two sets of numerical results is obtained. In this study, simulations are conducted for a much wider range of reduced velocity, and the vibration amplitude increases with the reduced velocity nearly linearly at $\beta = 90^{\circ}$ until $U_r = 20$. The vibration amplitudes for r = 0.5 are smaller than those for r = 0.32.

The enhancement of the vibration by the mechanically coupled rotation is due to the Magnus effect that causes a net lift force on a rotating cylinder placed in a fluid flow (Prantl 1926; Swanson 1961). The net lift force increases with the increase of the rotating

speed. If the flow approaches the cylinder at $\beta = 90^{\circ}$, then the upward motion of the cylinder causes the cylinder to rotate in the clockwise direction. The direction of the lift coefficient of a rotating cylinder in the clockwise direction caused by Mingus effect is in the same direction as the displacement; as a result, it further enhances the upward motion of the cylinder. Similarly, the negative Magnus-effect-caused downward lift coefficient when the cylinder moves downwards further enhances the downward motion. The above mechanism is the typical mechanism of galloping. Vicente-Ludlam, Barrero-Gil & Velazquez (2018) defined this type of response galloping. They experimentally tested VIV of a circular cylinder in the crossflow direction under two coupled rotation conditions: condition 1 where the rotation angle is proportional to the translational displacement of the cylinder, i.e.

$$\theta = k_1 X,\tag{3.1}$$

and condition 2 where the rotation angle is proportional to the translational velocity of the cylinder (\dot{X}) , i.e.

$$\theta = k_2 \dot{X}. \tag{3.2}$$

The correlation between θ and X is $\theta = X/r$ for the coupled configuration in figure 1. Equation (3.1) is equivalent to a coupled system with $r = -1/k_1$, considering that the direction of θ in this study is opposite to that defined by Vicente-Ludlam $et\ al.$ (2018). The mass ratio, the damping ratio and the Reynolds numbers in the experiments of Vicente-Ludlam $et\ al.$ (2018) are $m^* = 11.7$, $\zeta = 0.0043$ and $Re = 1500-10\ 000$, respectively. Positive and negative values of k_1 in (3.1) are equivalent to $\beta = -90^\circ$ and $\beta = 90^\circ$, respectively. Vicente-Ludlam $et\ al.$ (2018) found that a negative value of k_1 enhances vibration, and found that for $k_1 = -1.875$ to $k_1 = 0$, the lock-in regime is widened and the maximum vibration amplitude in the lock-in regime is increased. However, at $k_1 = -2.125$ (equivalent to r = 0.471), the cylinder's amplitude increases with the increase of the reduced velocity without stopping.

Nitti *et al.* (2022) have investigated the effects of rotation radius on the response for a constant flow direction $\beta = 90^{\circ}$, and found that r = 0.32 has the maximum amplitude. In this study, it is also proved that the vibration amplitude at r = 0.32 is much higher than amplitudes at r = 0.5 in figure 2. We will focus on the effects of the flow direction on the response for a constant rotation radius r = 0.32 in the rest of this paper.

A mesh dependency test is conducted to ensure that the mesh is sufficient dense for accuracy. In addition to the mesh that is used in all the simulations, a coarser mesh and a denser mesh are used to do the simulations for the case $\beta = 90^{\circ}$ and $U_r = 20$, where the vibration amplitude is the maximum. The properties of the meshes are listed in table 1, where W and H are the width and height of the computational domain, respectively, Nc is the number of finite elements on the cylinder surface, and Δ_{min} is the minimum mesh size in the radial direction on the cylinder surface. Figure 3 shows the time histories of the vibration displacements calculated from the three meshes; the vibration is periodic for all three meshes. The error e(V) in the table is defined as the difference between the result of any value presented by V and the result from the denser mesh, i.e. $e(V) = (|V - V_{denser\ mesh}|/V_{denser\ mesh}) \times 100\%$. It can be seen from table 1 that the difference between the amplitudes of the normal and denser meshes has been very small, indicating the convergence of the mesh. The difference in frequency (f) between the normal and denser meshes is smaller. The effect of the computational domain on the results is also checked by simulating the vibration with a larger computational domain and same mesh density as the normal mesh. The length and width of the larger domain are 1.5 times those in the normal mesh. The results for the larger domain shown in table 1

Mesh	W	H	Nc	Δ_{min}	A	E(A)	f	<i>e</i> (<i>f</i>)
Denser	60	100	160	0.0005	12.572	_	0.04458	_
Normal	60	100	120	0.001	12.626	0.43 %	0.04450	0.18 %
Coarser	60	100	96	0.0015	12.479	1.17 %	0.04459	0.21 %
Larger domain	90	150	120	0.001	12.183	2.35 %	0.04410	1.11 %

Table 1. Non-dimensional vibration amplitude and frequency for $\beta = 90^{\circ}$ and $U_r = 20$.

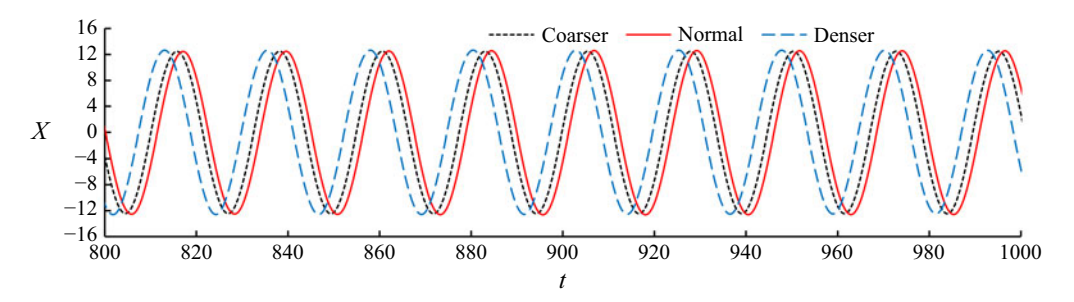


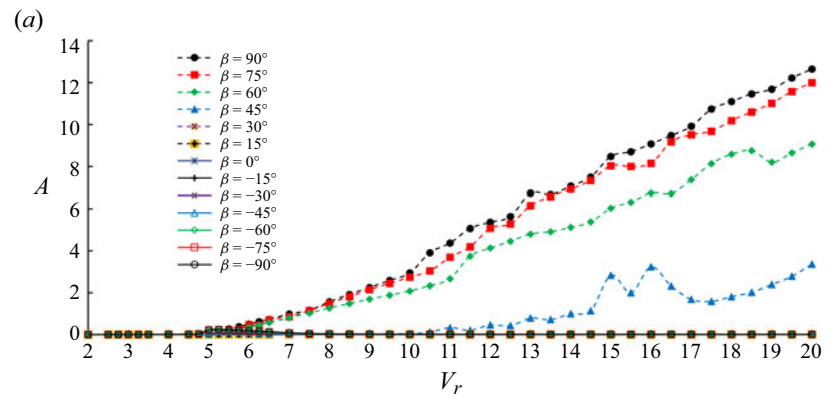
Figure 3. Comparison between the vibration time histories from three difference meshes.

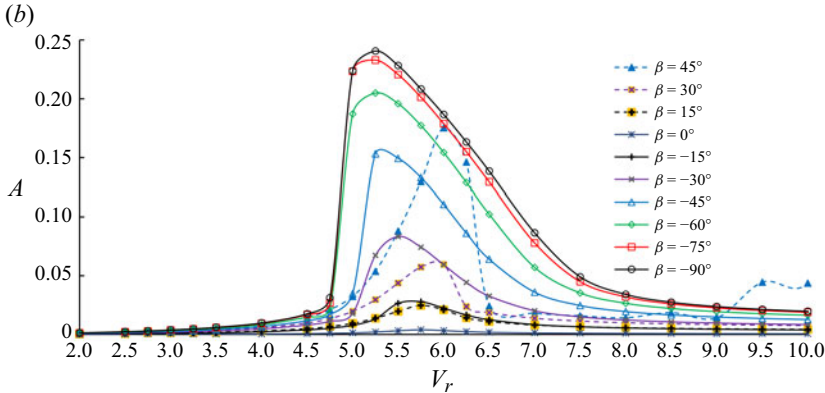
have very small differences from the normal mesh results. The amplitude of the larger domain's amplitude is 2.35 % greater than that of the normal mesh.

4. Results

Figure 4 shows the variation of the vibration amplitude with the reduced velocity for all the simulated flow direction angles. The vibration amplitude for $\beta = 45^{\circ}-90^{\circ}$ does not stop increasing with the increase of the reduced velocity until $V_r = 20$. This is a typical galloping response, which is self-excited instability with high amplitude and low frequency (Joly, Etienne & Pelletier 2012). Galloping is a classical instability mechanism in which a small transverse body motion creates an aerodynamic force that increases the motion (Bearman *et al.* 1987; Luo, Chew & Ng 2003). Galloping does not occur for structures with circular cross-sections if they do not rotate. However, the mechanical coupling between the vibration with the rotation motion of the cylinder creates the condition for galloping.

When the flow approaching angle is $\beta = -90^{\circ}$, an upward motion of the cylinder causes a downward Magnus lift force that has a damping effect on the vibration. As a result, galloping ceases and the vibration amplitude at $\beta = -90^{\circ}$ is much lower than that of a nonrotating cylinder, as illustrated in figure 4. Lu *et al.* (2011) and Vicente-Ludlam *et al.* (2018) utilised oscillatory rotation of a circular cylinder as an active control method to suppress FIV. The suppression mechanism in these two studies is the same as the one in this study at $\beta = -90^{\circ}$. In Lu *et al.* (2011), the rotation speed of the cylinder was proportional to the lift coefficient instead of the displacement cylinder, and achieved successful VIV suppression. Vicente-Ludlam *et al.* (2018) found that a rotation that follows (3.2) suppressed the VIV better than one that follows (3.1). When the angle of attack is between 45° and 90°, galloping is found, and the vibration amplitude during galloping is found to increase with the increase of flow direction angle in figure 4. For $-90^{\circ} \le \beta \le 30^{\circ}$, galloping is not found, but a distinct lock-in regime is identified in figure 4(c).





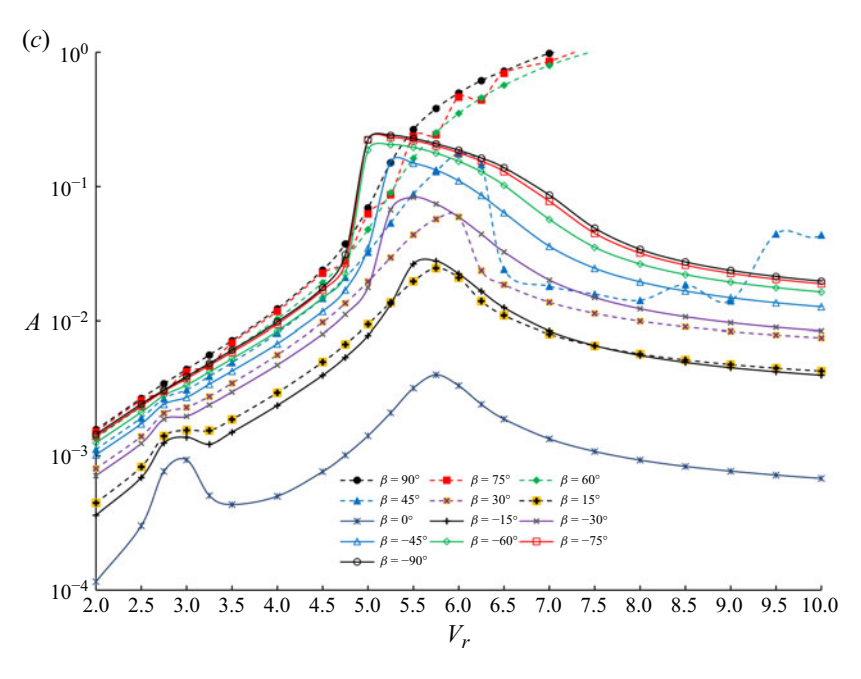
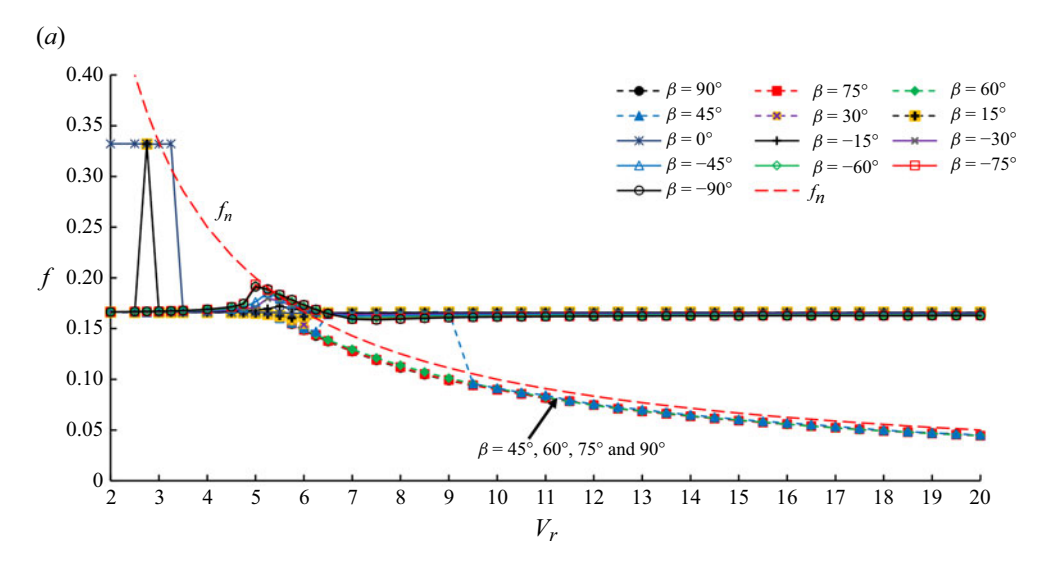


Figure 4. Variation of the vibration amplitude with the reduced velocity for Re = 100, $m^* = 8$ and r = 0.32. (a) Global view, (b) Zoomed-in view of the lock-in range and (c) Logarithmic scale of the A-axis.



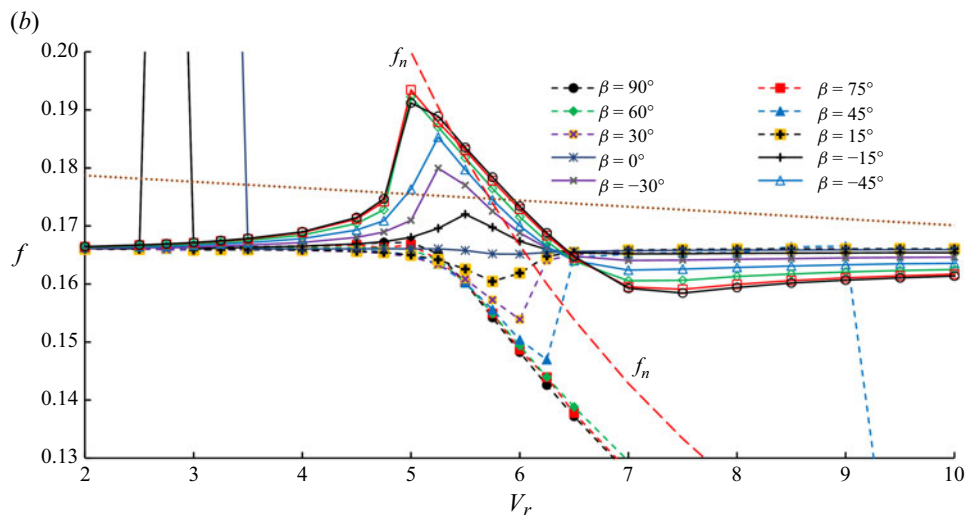


Figure 5. Variation of the vibration frequency with the reduced velocity. (a) Global view and Same as (b) with zoomed-in view near the Strouhal frequency.

Figure 5 shows the variations of the vibration frequency with the reduced velocity for all the simulated flow direction angles. The vortex shedding frequency of a non-rotating, stationary cylinder (referred to as the Strouhal number hereafter) is f = 0.166. At $\beta = 0^{\circ}$, where the cylinder vibrates in the in-line direction with a very small amplitude, the frequency is twice the Strouhal frequency because the drag force has a frequency twice the Strouhal frequency. For all the values of β , the vibration frequency is found to deviate from the Strouhal number, and the vibration amplitude increases gradually as the reduced velocity increases from 2 to 4.75 in figure 5(b). When the angle β is negative, the sudden increase in the response frequency is found to occur at $V_r = 5$ for $\beta = -90^{\circ}$ to $\beta = -60^{\circ}$, and these sudden increases are accompanied by a sudden increase in the vibration amplitude in figure 4. At $\beta = -30^{\circ}$, this sudden increase of the vibration

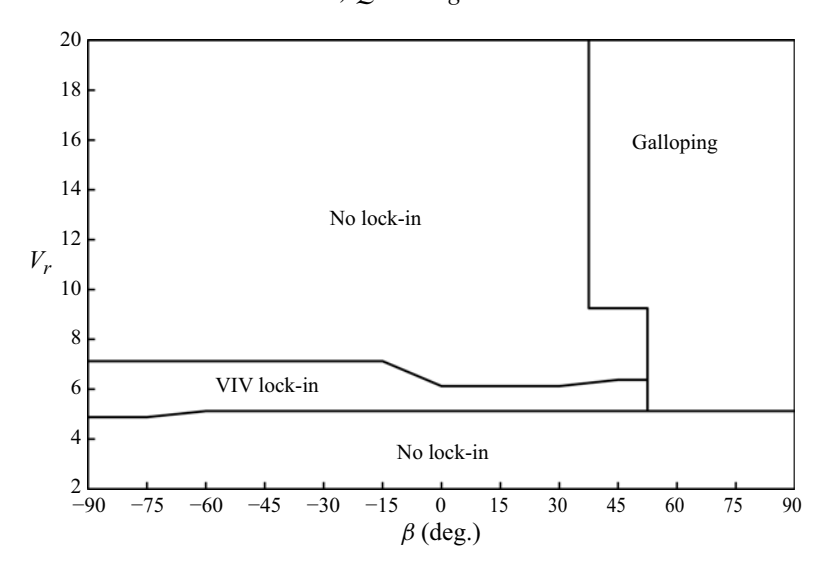


Figure 6. Mapping of lock-in regimes in the β – V_r plane.

frequency and amplitude occurs at $V_r = 5.25$. At $\beta = -15^\circ$, the vibration frequency smoothly increases to its maximum value with the increase of V_r until $V_r = 5.5$. For negative β values, the vibration frequency reduces with the increase of V_r after it increases to its maximum value. For positive $\beta = 15^\circ - 45^\circ$, the vibration frequency decreases with the increase of V_r until its minimum value, then jumps to the value close to the Strouhal number. At $\beta = 45^\circ$, the vibration is locked in between $V_r = 5.25$ and $V_r = 6.5$ because the vibration amplitudes are significantly different from those outside the lock-in regime, the frequency of the force is the same as the frequency of the vibration, and the vibration frequency follows the trend of f_n , instead of following the Strouhal frequency. At $\beta = 45^\circ$, the vibration is galloping when is V_r is greater than 5.5 because the vibration amplitude starts to increase with the increase of reduced velocity, as seen in figure 4(b), and the vibration frequency deviates from the Strouhal frequency.

Lock-in is defined as the response of the cylinder with high response amplitude and the matching between the vortex shedding frequency and the vibration frequency (Khalak & Williamson 1999; Navrose & Mittal 2016). Outside the lock-in regime, the vortex shedding frequency and vibration frequency follow the vortex shedding frequency of a stationary cylinder (Navrose & Mittal 2016). Based on the definition of lock-in, the lock-in regimes are mapped on the $\beta - V_r$ plane in figure 6. In figure 4(c), the local maximum value of the vibration amplitude at $V_r = 3$ for $\beta = 0^\circ$ and $\pm 15^\circ$ is not identified as lock-in, because the vibration amplitude is extremely small (less than 0.002).

The response is classified into two types: VIV lock-in and galloping. In the VIV lock-in regime, the vibration frequency and the frequency of the lift coefficient are the same, while in the galloping regime, the vibration frequency remains slightly lower than the natural frequency, but the frequency of the lift coefficient increases with the increase of the reduced velocity. It is interesting that the angle $\beta = 45^{\circ}$ has both VIV lock-in and galloping regimes, and these two regimes are separated from each other. The separation of the VIV regime from the lock-in regime was also reported for FIV of a square cylinder (Cui *et al.* 2015; Ji *et al.* 2024).

Figure 7 shows the variation of the response amplitude and frequency with the reduced velocity in the lock-in regimes with $\beta = -60^{\circ}$ and 45°. For $\beta = -60^{\circ}$, the lock-in regime has a very narrow initial branch and wide lower branch, while for $\beta = 45^{\circ}$, the lock-in

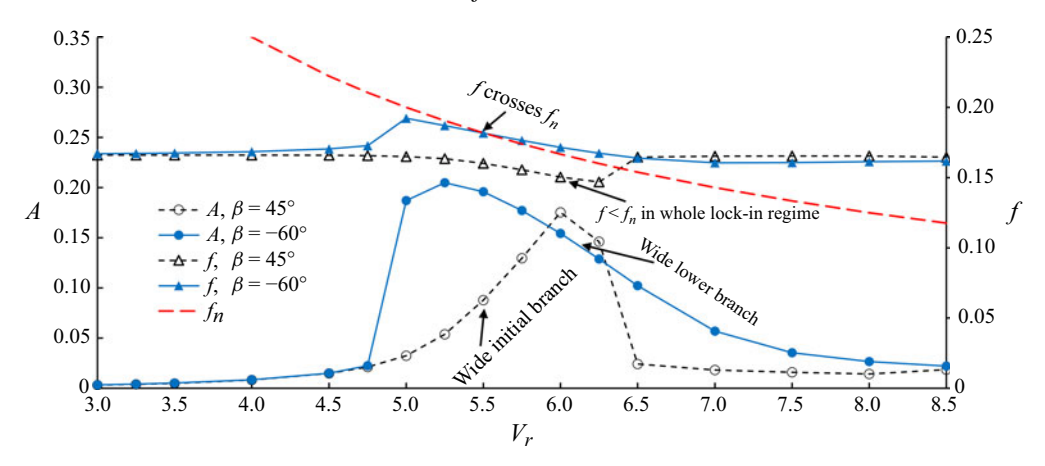


Figure 7. Difference between the lock-in regimes at $\beta = 45^{\circ}$ and $\beta = -60^{\circ}$.

regime has a very wide initial branch and a very narrow lower branch. Within the lock-in regime, the vibration frequency crosses the natural frequency at a certain V_r for $\beta=-60^\circ$, while it is always smaller than f_n for $\beta=45^\circ$. Lock-in regimes for $\beta=-60^\circ$ are similar to those of a non-rolling cylinder reported previously (Ji *et al.* 2011). The vibration frequency at $\beta=45^\circ$ approaches f_n , and the response amplitude increases gradually with the increase of the reduced velocity. It is the closest to f_n at $V_r=6.25$, and suddenly increases to a value close to the Strouhal frequency at $V_r=5$, where the lock-in ends.

In the galloping regime, the response amplitude increases continuously with the increase of the reduced velocity until the largest simulated V_r . The maximum amplitude in the lockin range of V_r is defined as peak amplitude A_p , and the vibration frequency corresponding to A_p is defined as peak frequency f_p . The variation of A_p and f_p/f_n with the flow direction angle β is shown in figure 8. Because the drag force caused by vortex shedding has much smaller amplitude than the lift force, the peak amplitude has the smallest value when the vibration is in the in-line direction at $\beta = 0^{\circ}$. An increase of $|\beta|$ in either the negative or positive direction increases the peak vibration amplitude. The peak frequency is found to be smaller than the natural frequency $(f_p/f_n < 1)$ in figure 8 for all values of β .

For an undamped system with spring constant K under an oscillatory external force, the equation of motion is $m\ddot{X} + K\dot{X} = F_0\cos(2\pi ft)$, and the theoretical solution is $X(t) = ((F_0/K)/(1-(f/f_n)^2))\cos(2\pi ft)$. The phase between the force $F_0\cos(2\pi ft)$ and the displacement X(t) changes from 0° to 180° respectively when f exceeds f_n . For a stabilised, undamped, periodic vibration, the phase should be either 0° or 180° since there is no energy exchange between the fluid and the cylinder. The phase may vary from period to period if there is a beating in the hysteresis region (Leontini, Thompson & Hourigan 2006; Jiang et al. 2024).

At high Reynolds numbers of the order of 10^3 – 10^4 , and low mass ratios, the lock-in range of the reduced velocity is divided into three branches: initial branch, upper branch and lower branch (Khalak & Williamson 1996). The upper branch does not exist for Reynolds numbers in the laminar regime (Singh & Mittal 2005; Ji *et al.* 2011). The initial branch is a very narrow branch where the vibration amplitude increases quickly to its maximum value with the increase of the reduced velocity. The vibration amplitude reaches its maximum at the upper branch, and drops at the boundary between the upper and lower branches, where $\Delta \psi$ changes from 0° to 180° .

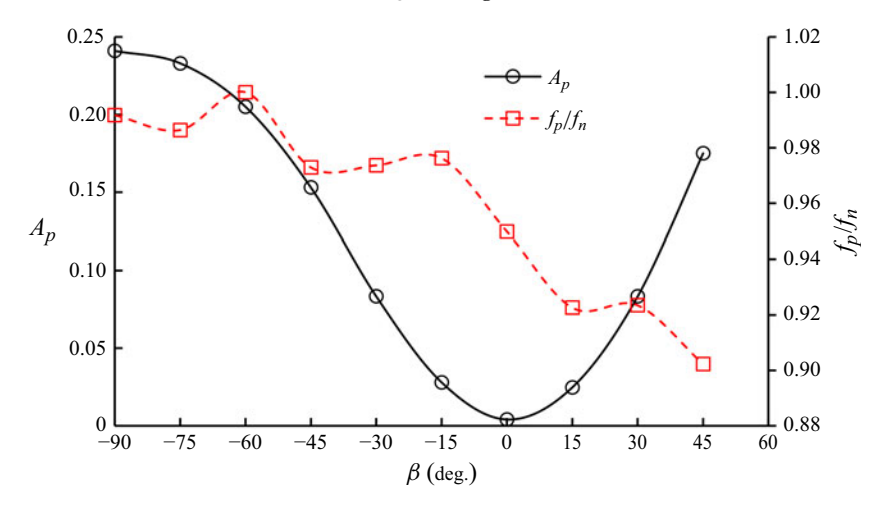


Figure 8. Variation of the peak amplitude in the lock-in regime with the angle of attack.

The 0° to 180° phase jump was found to be at the boundary between the upper and lower branches at low mass ratios and Reynolds numbers between 10^{3} and 10^{4} (Khalak & Williamson 1999; Sarpkaya 2004). Since the damping ratio is zero in this study, the phase (referred to as ψ) between the vibration displacement and the equivalent force F_{e} should be either 0° or 180° .

When galloping occurs, the force coefficient in the vibration direction has multiple frequencies, and the high frequency components are caused by the vortex shedding. The vibration is excited by the force component whose frequency is the same as the vibration frequency. To determine the phase between vibration and force, the vibration displacement and the force coefficient are decomposed into harmonics:

$$X(t) = X_0 + \sum_{n=1}^{N} X_n \sin(2\pi n f + \psi_{x,n}), \tag{3.3}$$

$$F_e(t) = F_{e0} + \sum_{n=1}^{N} F_{e,n} \sin(2\pi n f + \psi_{Fe,n}), \tag{3.4}$$

where $\psi_{x,n}$ and $\psi_{Fe,n}$ are the phases of the *n*th harmonics of X and F_e , respectively. The phase difference between the first harmonics of X and F_e is defined as $\Delta \psi = \psi_{Fe,1} - \psi_{Fe,1}$. Figure 9 shows the variation of $\Delta \psi$ with reduced velocity for all the β angles. When there is a lock-in regime ($\beta = -90^\circ$ to $\beta = 45^\circ$), the phase $\Delta \psi$ changes from 0° to 180° at a critical V_r , which increases with the increase of β . When there is only a galloping regime ($\beta = 60^\circ$ and 90°), the phase difference $\Delta \psi$ remains 0° until the largest simulated $V_r = 20$. It is interesting to see that at $\beta = 45^\circ$, $\Delta \psi$ changes to 180° in the lockin regime, and changes back to 0° in the galloping regime. Within the lock-in regime, the frequency is always lower than f_n at $\beta = 45^\circ$ because $\Delta \psi$ does not change from 0° to 180° . At $\beta = 0^\circ$, the phase changes from 0° to 180° at $V_r = 3.25$, and changes back to 0° at $V_r = 3.5$, because the vibration is driven by the drag coefficient, whose frequency is twice the Strouhal frequency (see figure 5a). It can be concluded that the condition of galloping is that the phase $\Delta \psi$ remains 0° .

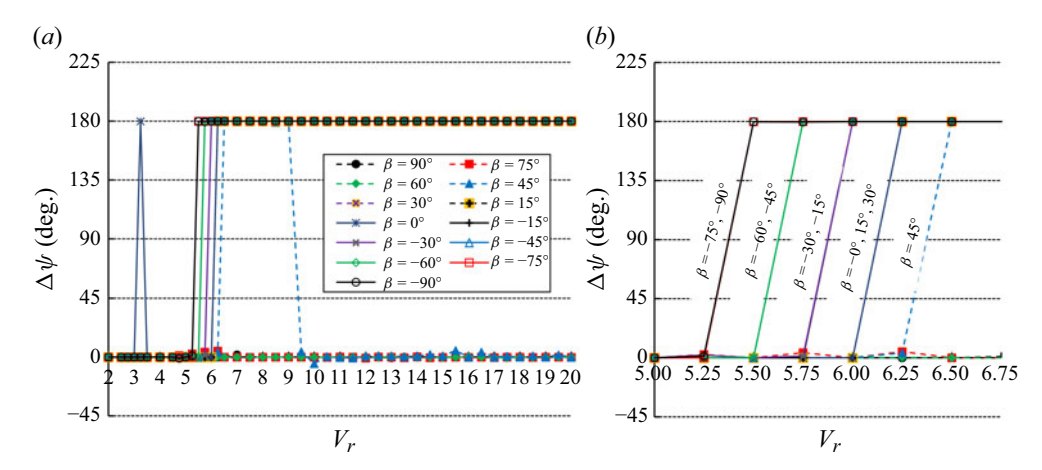


Figure 9. Variation of the phase difference between the vibration displacement and equivalent force F_e with the reduced velocity.

Since the vibration is driven by the combination of both lift force and the torque without damping, the net exchange between the effective force F_e and the vibration must be zero to maintain stable vibration with constant frequency and amplitude. The roles of the force and torque on exciting/damping the vibration are quantified by the power that they have towards the cylinder. The non-dimensional powers supplied by the force and torque are represented by E_F and E_T , respectively, and they are calculated by

$$E_F = C_F V = \frac{\hat{F}_X \hat{V}}{\frac{1}{2} \rho D U^3},$$
(3.5)

$$E_T = C_T \sigma = \frac{\hat{T}_\theta \hat{\sigma}}{\frac{1}{2} \rho D U^3},\tag{3.6}$$

where $V=\dot{X}$ is the non-dimensional velocity of the cylinder, σ is the non-dimensional rotation speed of the cylinder, and the force coefficient C_F in the X-direction and the torque coefficient C_T are defined by $C_F=\hat{F}_X/((1/2)\rho DU^2)$ and $C_T=\hat{T}_\theta/((1/2)\rho D^2U^2)$, respectively. The time-averaged power done by the force and torque are defined as \overline{E}_F and \overline{E}_T , respectively. Figure 10(a,b) show the variations of \overline{E}_F and \overline{E}_T with the reduced velocity for some exemplar cases to demonstrate that \overline{E}_F and \overline{E}_T have same magnitude but opposite signs, proving that the net power exchange between fluid and cylinder is zero. Fluid force damps the vibration instead of providing power to the cylinder in some cases. For example, in figure 10(a), \overline{E}_F is negative between $V_r=2$ and $V_r=5.25$ for $\beta=15^\circ$, and between $V_r=5$ and $V_r=7$ for $\beta=0^\circ$, indicating that the fluid force damps the vibration. The magnitudes of \overline{E}_F and \overline{E}_T are correlated to the vibration amplitude. In figure 10(c), the values of \overline{E}_F and \overline{E}_T for large-amplitude galloping vibration for $\beta=75^\circ$ and 90° are a number of orders greater than their values for the small-amplitude VIV for $\beta=15^\circ$ and 0° . The powers of \overline{E}_F and \overline{E}_T for $\beta \leq 30^\circ$ are too small to be seen when they are plotted together with larger values of β in figure 10.

Figure 11(a) maps the roles of fluid force and torque in VIV on the β – V_r plane, and figure 11(b) shows the contours of \overline{E}_F on the β – V_r plane. The whole plane is divided into four zones: two A zones, where fluid force supplies power to vibration while the fluid torque extracts the power from the vibration, and two B zones, where the roles of

M. Zhao, Q. Zhang and Y. Liu

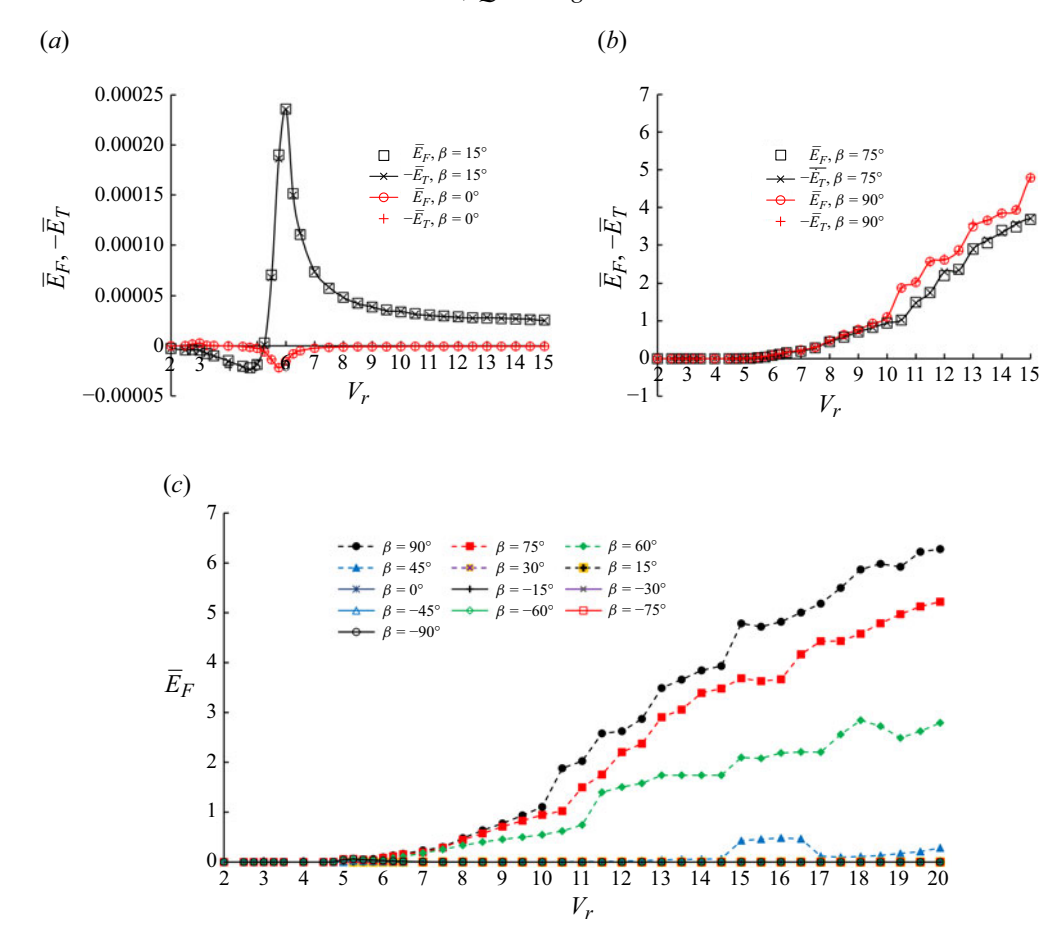


Figure 10. Variation of the power by the force and the torque with the reduced velocity. (a) \overline{E}_F and \overline{E}_T , $\beta=15^\circ$ and 0° , (b) \overline{E}_F and $-\overline{E}_T$, $\beta=75^\circ$ and 90° and (c) \overline{E}_F only, $\beta=-90^\circ$ to 90° .

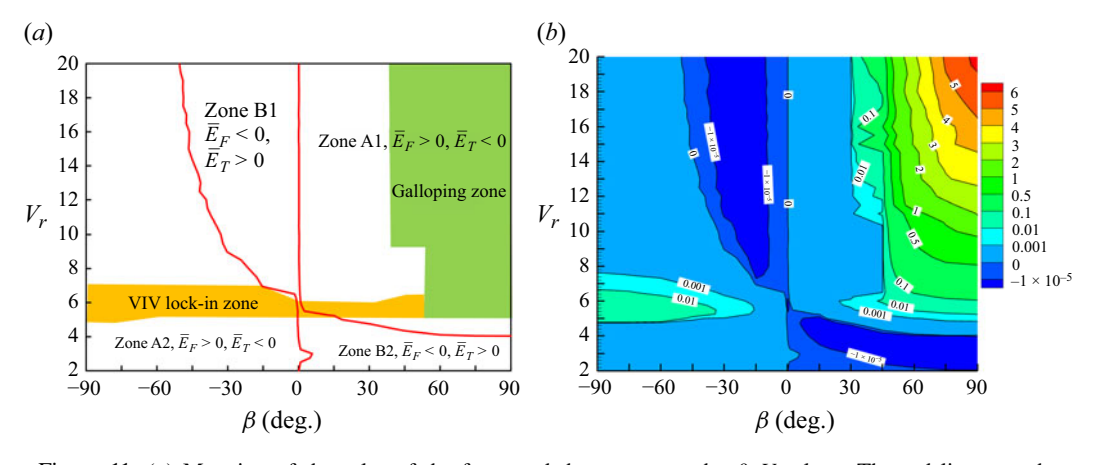


Figure 11. (a) Mapping of the roles of the force and the torque on the β – V_r plane. The red lines are the boundaries between zones A1, A2, B1 and B2. The coloured areas are the galloping and VIV lock-in regimes, respectively. (b) Contours of \overline{E}_F on the β – V_r plane.

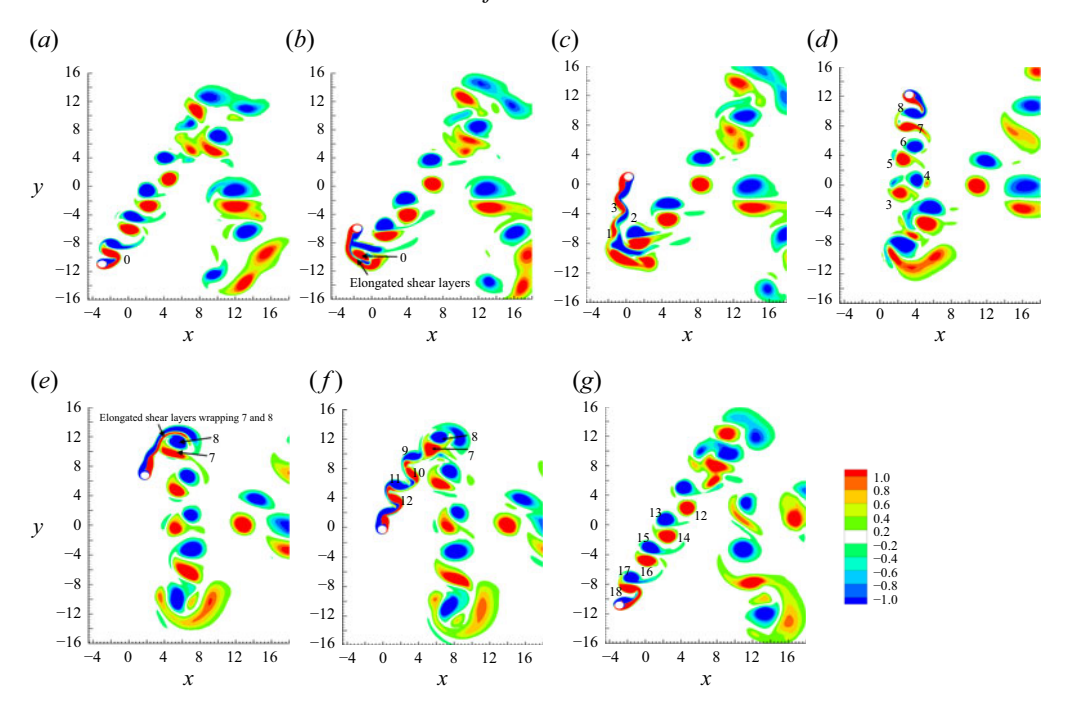


Figure 12. Vortex shedding in the galloping regime at $\beta = 75^{\circ}$ and $V_r = 20$. (a) t = 603.72, $X = X_{min}$, (b) t = 607.26, (c) t = 609.60, (d) t = 614.82, $X = X_{max}$, (e) t = 618.60, (f) t = 620.82 and (g) t = 625.86, $X = X_{min}$.

fluid force and torque swap (see figure 11a). The red lines are the boundaries between these zones. The VIV lock-in regime and the galloping regime are mapped into figure 11 using coloured areas. It can be concluded from figure 11 that galloping and VIV lock-in are excited by fluid force $(\overline{E}_F > 0)$ except for $\beta = 0^\circ$, while fluid torque can only excite very weak vibration outside VIV lock and galloping regimes. The VIV lock-in regime for $\beta = 0^\circ$ is in the zone with $\overline{E}_F < 0$; however, the peak amplitude of VIV lock-in at this angle is negligibly smaller than for other angles (see figure 8). The roles of the fluid force in exciting/damping vibration at positive β values are opposite to their roles at negative β values. When $\beta > 0^\circ$, fluid force excites vibration at large V_r above the red line in figure 11(a) $(\overline{E}_F > 0)$, and damps the vibration at small V_r , while when $\beta < 0^\circ$, flow force excites vibration at small V_r below the red line. The two zones where fluid torque excites vibration $\overline{E}_T > 0$ in figure 11(b) have negligible smaller $|\overline{E}_F|$ than the zones with $\overline{E}_F > 0$. As per figure 11(a), fluid torque can excite vibration only outside the lock-in and galloping zones.

Figure 12 shows the vortex shedding process within one period of vibration in the galloping regime for $\beta = 75^{\circ}$ and $V_r = 20$. The instants when the cylinder reaches its maximum and minimum X-positions, represented as X_{max} and X_{min} , respectively, are treated as the starting time of a half-period in the discussion. The vortices that are shed from the cylinder are labelled by numbers in the figure. In figure 12(a), where the cylinder is at its smallest X-position ($X = X_{min}$), vortex 0 is the last vortex that was shed from the previous period. Immediately after the cylinder changes its moving direction at $X = X_{min}$, the shear layers separated from the cylinder elongate and wrap around the last two vortices that are shed in the previous half-period, instead of forming vortices, until t = 607.26.

Figure 12(b-d) illustrate that eight vortices are shed from the cylinder while the cylinder is moving from $X = X_{min}$ to $X = X_{max}$. After the cylinder reaches X_{max} , vortex shedding does not form until 618.60 in figure 12(e). In the half-period where the cylinder moves from X_{max} to X_{min} , ten vortices are shed from the cylinder (see figure 12(e-g)). The number of vortices that are shed from the first half-period is one pair less that from the second half-period because the velocity of the fluid flow relative to the cylinder in the first halfperiod is lower when the cylinder is vibrating diagonally. Because of the difference in the relative flow velocity, vortex shedding in the first half-period starts later than in the second half-period, relative to the time when the cylinder changes it motion direction at either X_{max} or X_{min} . Because the cylinder vibrates nearly in the vertical direction with large amplitude, the vortices in the wake are aligned diagonally in a zigzag shape. For flow past a rotating circular cylinder, vortex shedding ceases when the rotation rate exceeds 1.8 for Re = 100 (Kang, Choi & Lee 1999). The maximum angular velocity for all the simulated cases occurs at $(\beta, V_r) = (90^\circ, 20)$ and the corresponding rotation rate $\alpha = \hat{\sigma} D/(2U) = 1.78$, which has not passed the critical rotation rate for vortex shedding to suppress.

5. Potential for energy harvesting using FIV

Nitti et al. (2022) recommended that the vibration of a circular cylinder mechanically coupled with rotation has great potential. When vibration is used for energy harvesting, a power generator receives energy and converts it to electricity. A damper for controlling vibration also receives energy and converts it to heat. Power generators and dampers have the same function of receiving energy from the vibration, but process the received energy differently. Many researchers added an additional linear damping coefficient in (2.1) to investigate the potential energy that can be harvested from the FIV (Chen et al. 2024; Zhang et al. 2024). Considering the damping coefficient that accounts for the harvested mechanical energy, the equation of motion (2.2) becomes

$$m^* e^{\frac{d^2 X}{dt^2}} + (C^* + C_e^*) \frac{dX}{dt} + K^* X = F^*,$$
 (3.7)

where $C_e^* = C_e/(\rho DU)$, and C_e is the energy harvesting damping coefficient due to the extraction of mechanical energy from the vibration. The parameter $C^* = 0$ is used to obtain the maximum possible energy to be harvested. The damping ratio for energy harvesting is defined as

$$\zeta_e = \frac{C_e}{2\sqrt{Kme}}.\tag{3.8}$$

Since the maximum amplitude occurs at $\beta = 90^{\circ}$ based on the previous section, the case $\beta = 90^{\circ}$ is considered when the energy harvesting is analysed. The time-averaged non-dimensional harvested power is the net power that transferred from the fluid to the cylinder:

$$\overline{E} = \overline{E}_F + \overline{E}_T. \tag{3.9}$$

In all the cases with $\beta = 90^{\circ}$, it is found that \overline{E}_F is positive and \overline{E}_T is negative, indicating that the fluid force provides power to the cylinder, and part of the power was used to rotate the cylinder. To validate the energy harvesting model, the simulated results for the case where the cylinder is not mechanical coupled ($C^* = 0$, $e = A/D^2$ and $F^* = \hat{F}_X/(\rho DU^2)$ in (3.7)) are compared with the results at Re = 150, $m^* = 2$, the reduced velocity $U_r = U/(f_N D) = 5.2$ and a wide range of ζ_e by Soti *et al.* (2017).

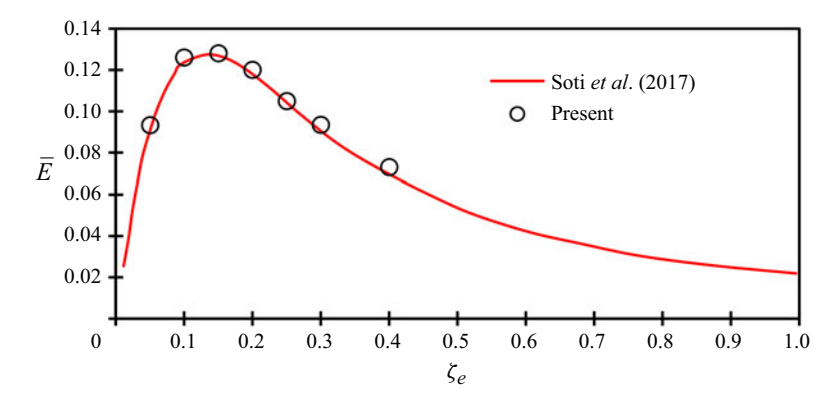


Figure 13. The comparison between the calculated non-dimensional power with the numerical results by Soti et al. (2017) at Re = 150, $m^* = 2$ and $V_r = 4.25$.

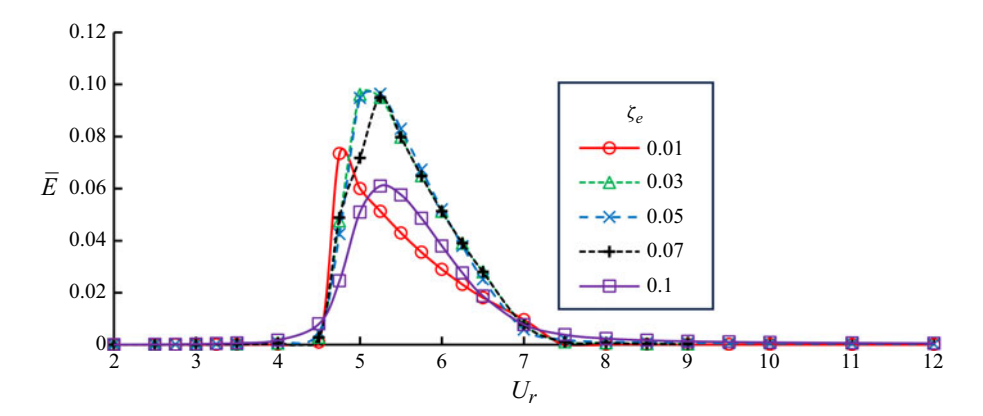


Figure 14. Variation of the non-dimensional power with the reduced velocity for a circular cylinder without mechanically coupled rotation at Re = 100 and $m^* = 8$.

Soti *et al.* (2017) defined the reduced velocity using the reduced velocity measured in fluid f_N considering the added mass coefficient $C_A = 1$ instead of f_n . The reduced velocity $U_r = 5.2$ is equivalent to $V_r = 4.25$. Figure 13 shows very good agreement between the present results and the results by Soti *et al.* (2017). The maximum non-dimensional power found in this study is 0.128, occurring at $\zeta_e = 0.15$. Simulations for Re = 100 and $m^* = 8$ without mechanically coupled rotation are conducted, and the powers for different ζ_e are shown in figure 14. The results for $\zeta_e = 0.03$ and 0.05 are very close to each other, and the maximum non-dimensional power is approximately 0.095. When ζ_e is less than 0.03 or greater than 0.05, the maximum non-dimensional power reduces.

Since the maximum vibration amplitude occurs at $\beta = 90^{\circ}$, the energy of a cylinder coupled with rotation at $\beta = 90^{\circ}$ is investigated for $\zeta = 0$, $\zeta_e = 0.01-0.1$, with increment 0.01. Figure 15 shows the time histories of the displacements of a cylinder normalised by the maximum displacements $|X|_{max}$ for $\zeta_e = 0.05$ and all the reduced velocities. The vibration with damping coefficient $\zeta_e = 0.05$ develops to equilibrium periodic stages very slowly. For example, the vibration becomes stable at t = 1200 at $V_r = 20$ if $\zeta_e = 0.05$, and at t = 700 if $\zeta_e = 0$. For some reduced velocities, such as $V_r = 9.5$ and $\zeta_e = 0.05$, the simulation needs to be run for t = 4000 to obtain the stable vibration stage. For a large-amplitude galloping case, the cylinder gains energy gradually for a long period of time

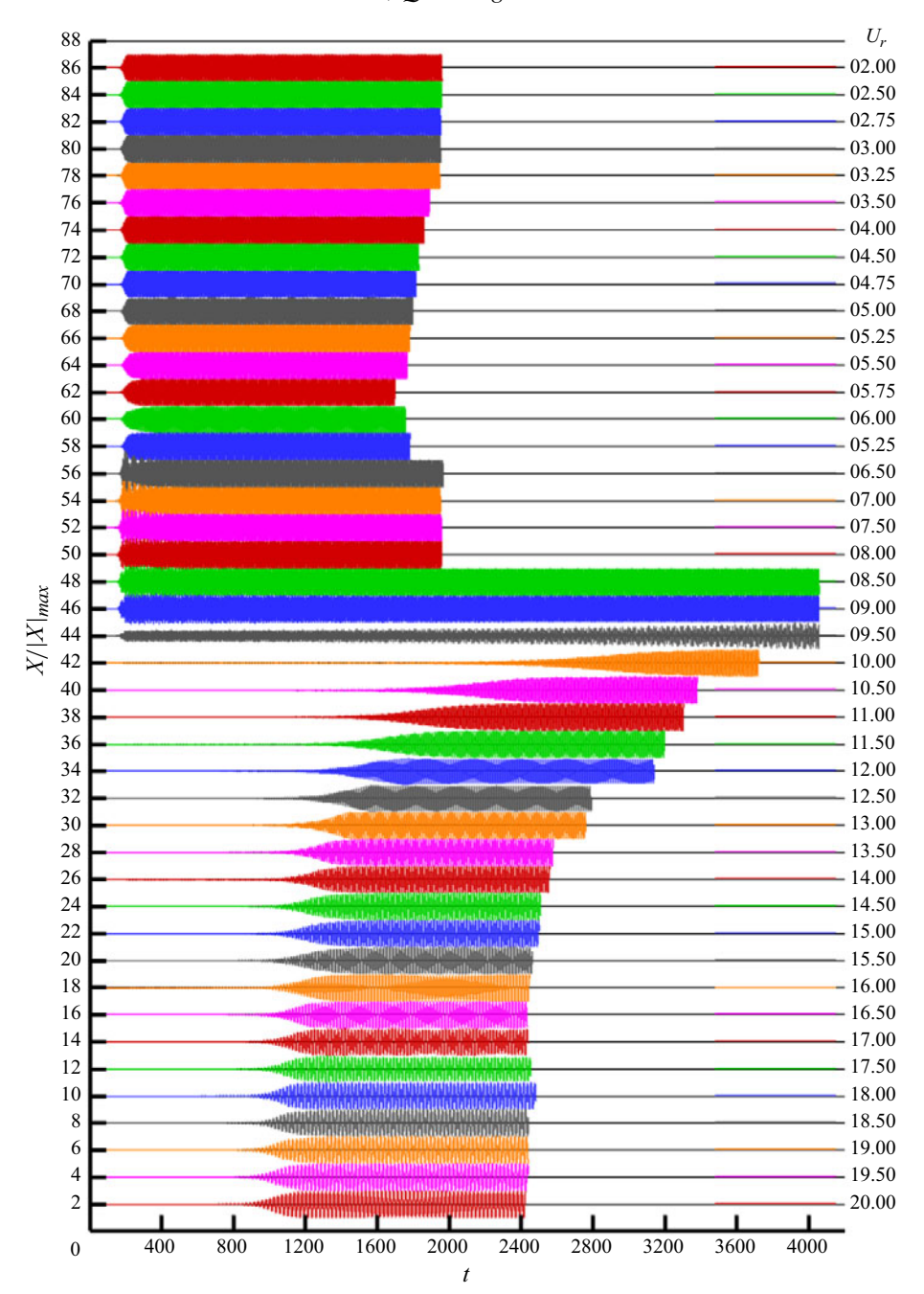
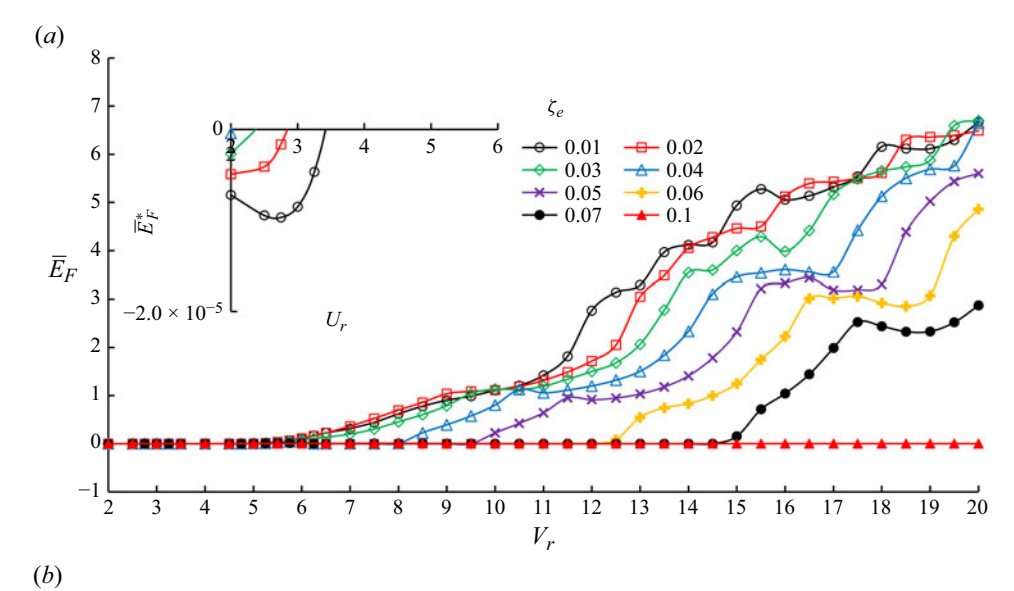


Figure 15. Time histories of the displacement *X* of a cylinder mechanically coupled with rotation r = 0.32 and $\zeta_e = 0.05$.

until the vibration amplitude stabilises. Considering that the damper consumes energy, the time for the cylinder to develop to stable condition for a damped case is longer than the case without damping.

Figure 16(a,b) show the variations of the non-dimensional power from fluid force and the power from fluid torque, respectively. Both \overline{E}_F and \overline{E}_T are very small at smaller



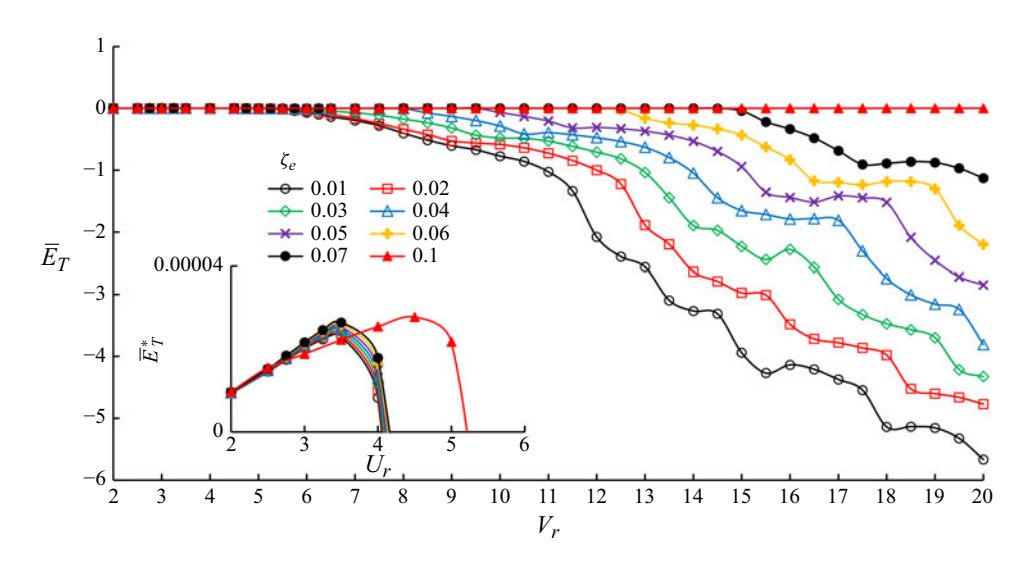


Figure 16. Contributions of fluid force and fluid torque on the power generation. (a) Force contribution \overline{E}_F and (b) Torque contribution \overline{E}_T .

reduced velocities, and the zoomed-in views at smaller reduced velocities are shown in the insets. One can observe that both \overline{E}_F and \overline{E}_T increase with the increase of V_r , but their signs are opposite at large reduced velocities. The contributions of \overline{E}_F and \overline{E}_T in energy harvesting can be identified more clearly in figure 17, where their signs are mapped on the ζ_e-U_r plane. When both ζ_e and V_r are very small, $\overline{E}_F<0$ and $\overline{E}_T>0$, indicating that fluid torque provides energy to the cylinder, and fluid force consumes energy. When $V_r \leq 4$, both fluid force and torque supply energy to the cylinder in large range of ζ_e in figure 17(a) because both \overline{E}_F and \overline{E}_T are positive. When $V_r \geq 4.5$ and for the whole range of ζ_e , fluid force supplies energy to the cylinder, $\overline{E}_F^*>0$, while fluid torque extracts energy from the cylinder, $\overline{E}_T<0$.

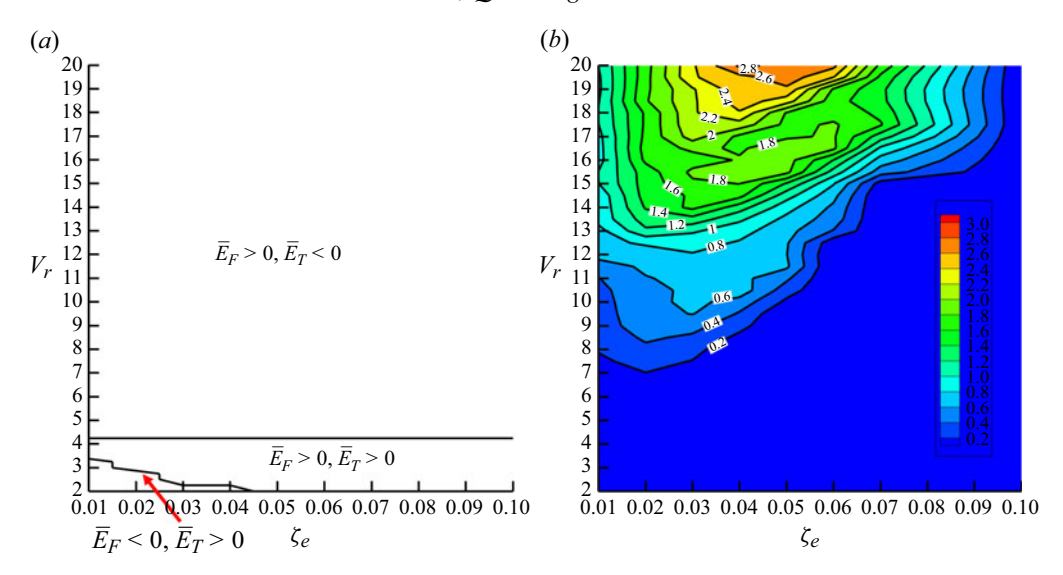
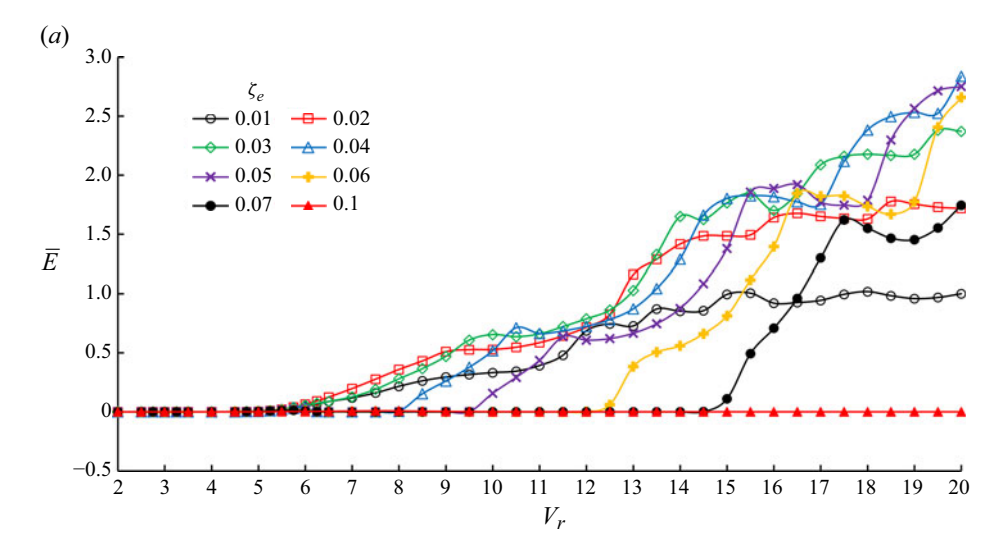


Figure 17. (a) Contributions of \overline{E}_F and \overline{E}_T in energy harvesting. (b) Contours of the non-dimensional power \overline{E} on the ζ_{ℓ} - V_r plane.

Figure 17(b) shows the contours of the harvested power from the fluid $\overline{E} = \overline{E}_F + \overline{E}_T$ on the $\zeta_e - U_r$ plane. The maximum \overline{E} is 2.8, which occurs at $\zeta_e = 0.04$ and $V_r = 20$, which is approximately 30 times the maximum \overline{E} for a non-rotating cylinder. The maximum \overline{E} is greater than 1 because the cylinder's large vibration amplitude harvests energy in a flow zone in the crossflow direction wider than one diameter.

Figure 18 shows the variation of E with the reduced velocity. The power E increases with the increase of V_r , with some oscillation in the galloping regime for all values of ζ_e . Damping coefficients $\zeta_e=0.03, 0.04$ and 0.05 appear to perform equally well in the energy harvesting, and they can achieve non-dimensional power between 2 and 2.5 at $V_r=20$. The maximum values of \overline{E} occurring between $V_r=5.5$ and 6 are found for $\zeta_e\geq0.04$, and the maximum value of \overline{E} is 0.036 at $V_r=6$ for $\zeta_e=0.04$. The peak power occurring between $U_r=5.5$ and 6 is negligibly smaller than the power at larger reduced velocities above 10; it can only be identified in figure 18(b) with a logarithmic \overline{E} -axis. For $\zeta_e\geq0.04$, \overline{E} reaches its maximum value at a reduced velocities between 5.5 and 6, reduces, and increases again at a critical reduced velocity, which is the lower boundary reduced velocity of the galloping regime. Lower boundary reduced velocities of galloping regimes are $V_r=8.5$, 10, 13 and 15 for $\zeta_e=0.04$, 0.05, 0.06 and 0.07, respectively, in figure 18, while galloping was not seen until $V_r=20$ at $\zeta_e=0.1$.

When the cylinder vibrates, the swept distance of the cylinder in the crossflow direction is $2\hat{A} + D$, where \hat{A} is the dimensional vibration amplitude. The available dimensional fluid power in the cylinder swept area is $\hat{P}_f = (1/2)(2\hat{A} + D)\rho U^3$, and the non-dimensional fluid power in the swept area is $P_f = \hat{P}_f/((1/2)D\rho U^3) = 2A + 1$. The efficiency η of energy harvesting is defined as the harvested power divided by the fluid power in the cylinder swept area $\eta = \overline{E}/P_f$. Figure 19 shows the contours of the energy harvesting efficiency on the $\zeta_e - V_r$ plane. The maximum efficiency over the whole range of simulated parameter space is 0.424, which occurs at $(\zeta_e, V_r) = (0.04, 20)$.



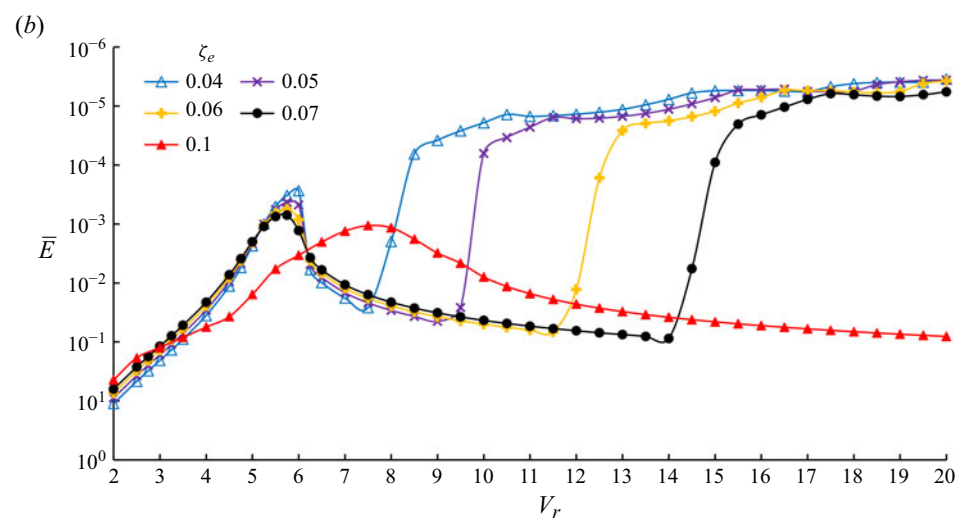


Figure 18. Variation of the non-dimensional power with the reduced velocity for various values of ζ_{ℓ} :
(a) linear scale \overline{E} -axis; (b) same as (a) except that the \overline{E} -axis uses a logarithmic scale.

6. Conclusions

The FIV of a circular cylinder mechanically coupled with rotation is investigated numerically for Re = 100, $m^* = 8$, r = 0.32, $-90^{\circ} \le \beta \le 90^{\circ}$, $2 \le V_r \le 20$. The coupled system proved effective in enhancing vibration at $\beta = 90^{\circ}$ (Nitti *et al.* 2022). In this paper, the effects of the flow direction angle β on the vibration are studied, and the potential of energy harvesting from the coupled system was proved. Since $\beta = 90^{\circ}$ and r = 0.32 are the optimal flow direction angle and rotational radius, respectively, for achieving the maximum vibration amplitude, they are used for the energy harvesting study.

Two types of lock-in are found: VIV lock-in, where the vibration and vortex shedding synchronise, and galloping, where the vibration amplitude increases with the increase of V_r without upper boundary. The vibration amplitude that the cylinder can achieve in the VIV regime is much smaller than in the galloping regime. The effect of the

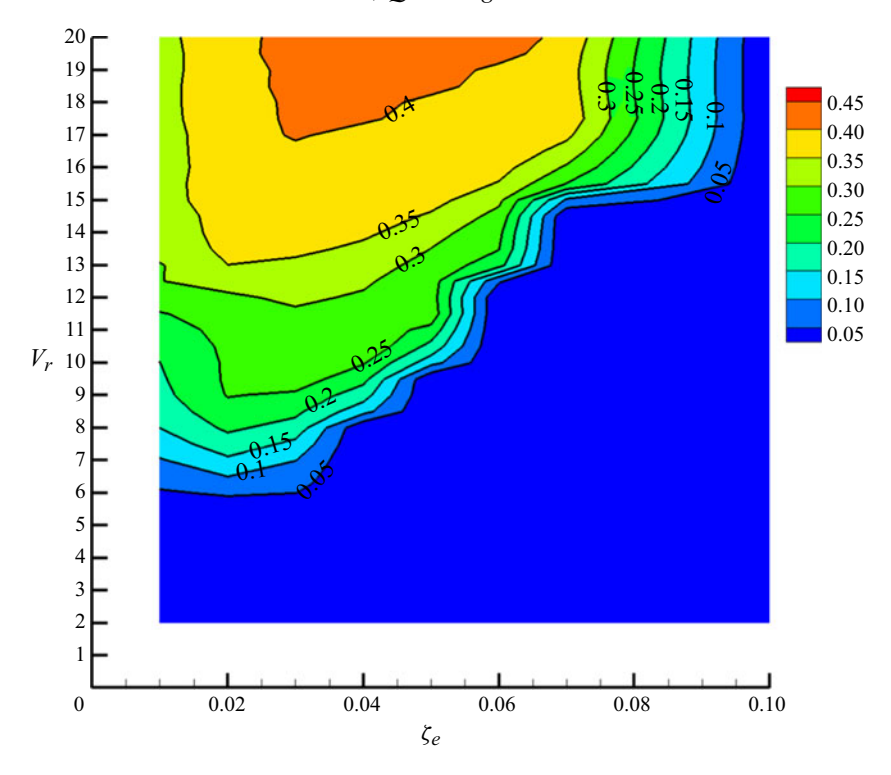


Figure 19. Contours of efficiency on the $\zeta_e - V_r$ plane.

flow approaching angle β relative to the direction of vibration is investigated. Both VIV response and galloping regimes are found at $\beta=45^{\circ}-90^{\circ}$; the response amplitude increases with the increase of the angle β in both regimes. For $\beta=-90^{\circ}$ to $\beta=0^{\circ}$, only VIV response regimes are found.

When the damping ratio is zero, fluid torque and force contribute to the vibration in opposite ways, and the net power transfer from the fluid to the cylinder through force and torque is zero. The β – V_r plane was divided into two type A zones, where fluid force power is $\overline{E}_F > 0$ and fluid torque power is $\overline{E}_T < 0$, and two type B zones, where $\overline{E}_F < 0$ and $\overline{E}_T > 0$. Both galloping and VIV regimes are excited by fluid force instead of fluid torque, and they are in type A zones. In the galloping regime, the number of vortices that are shed from the cylinder increases with the increase of the vibration amplitude. At large amplitude and when the cylinder vibrates nearly vertically, the vortex street is aligned in a zigzag pattern because of the strong vibration.

Energy harvesting from FIV is investigated through an electrical damping coefficient ζ_e at $\beta=90^\circ$ where the vibration amplitude achieves its maximum compared with other flow direction angles. The energy harvesting power in the galloping regime increases with the increase of reduced velocity. The energy harvesting power in the VIV regime is negligibly smaller than in the galloping regime. Damping coefficients $\zeta_e=0.03, 0.04$ and 0.05 perform equally well in the energy harvesting, and they can achieve non-dimensional power between 2 and 2.5 at $V_r=20$, which is over 30 times the maximum achievable power of a non-rotating cylinder. The energy harvesting efficiency is defined as the ratio of the harvested energy to the available flow energy in the cylinder swept area. The maximum efficiency over the whole range of simulated parameter space is 0.424, which occurs at $(\zeta_e, V_r)=(0.04, 20)$.

The $\zeta_e - V_r$ space (see figure 17a) can be divided into three zones based on the contributions of fluid force and torque on energy harvesting: force and torque damp and provide energy, respectively, in zone 1 (both V_r and ζ_e are small), both force and torque provide energy in zone 2 (V_r is below 4), and force supplies energy and torque damps energy in zone 3 (V_r is above 4). The high-power galloping regime is in zone 3.

Declaration of interests. The authors report no conflict of interest.

REFERENCES

- BEARMAN, P.W., GARTSHORE, I.S., MAULL, D.J. & PARKINSON, G.V. 1987 Experiments on flow-induced vibration of a square-section cylinder. *J. Fluids Struct.* 1, 19–34.
- CHEN, W., LI, X. & YANG, W. 2024 Shape optimization to enhance energy harvesting from vortex-induced vibration of a circular cylinder. *Phys. Fluids* 36, 023612.
- Cui, Z., Zhao, M., Teng, B. & Cheng, L. 2015 Two-dimensional numerical study of vortex-induced vibration and galloping of square and rectangular cylinders in steady flow. *Ocean Engng* **106**, 189–206.
- HONG, K.S. & SHAH, U.H. 2018 Vortex-induced vibrations and control of marine risers: a review. Ocean Engng 152, 300–315.
- JI, C., XIAO, Z., WANG, Y. & WANG, H. 2011 Numerical investigation on vortex-induced vibration of an elastically mounted circular cylinder at low Reynolds number using the fictitious domain method. *Intl J. Comput. Fluid Dyn.* 25, 207–221.
- JI, C., ZHANG, D., YAO, Y., LI, W. & ZHANG, S. 2024 Flow-induced vibration of a square cylinder in low-Re flows: excitation mechanisms at different mass ratios. Ocean Engng 294, 116723.
- JIANG, H., JU, X., ZHAO, M., ZHOU, T., DRAPER, S., AN, H., WATSON, P., LEI, Z. & WANG, L. 2024 Large-eddy simulation of vortex-induced vibration of a circular cylinder at Reynolds number 10 000. *Phys. Fluids* 36, 085113.
- JOLY, A., ETIENNE, S. & PELLETIER, D. 2012 Galloping of square cylinders in cross-flow at low Reynolds numbers. J. Fluids Struct. 28, 232–243.
- KANG, S., CHOI, H. & LEE, S. 1999 Laminar flow past a rotating circular cylinder. *Phys. Fluids* 11, 3312–3321.
- KHALAK, A. & WILLIAMSON, C.H.K. 1996 Dynamics of a hydroelastic cylinder with very low mass and damping. J. Fluids Struct. 10, 455–472.
- KHALAK, A. & WILLIAMSON, C.H.K. 1999 Motions, forces and mode transitions in vortex-induced vibrations at low mass-damping. *J. Fluids Struct.* 13, 813–851.
- LEONTINI, J.S., THOMPSON, M.C. & HOURIGAN, K. 2006 The beginning of branching behaviour of vortexinduced vibration during two-dimensional flow. *J. Fluids Struct.* 22, 857–864.
- LU, L., QIN, J.M., TENG, B. & LI, Y.C. 2011 Numerical investigations of lift suppression by feedback rotary oscillation of circular cylinder at low Reynolds number. *Phys. Fluids* 23, 033601.
- LUO, S.C., CHEW, Y.T. & NG, Y.T. 2003 Hysteresis phenomenon in the galloping oscillation of a square cylinder. J. Fluids Struct. 18, 103–118.
- MUNIR, A., ZHAO, M., WU, H. & TONG, F. 2021 Flow-induced vibration of a rotating circular cylinder at high reduced velocities and high rotation rates. *Ocean Engng* 238, 109562.
- NAVROSE, N. & MITTAL, S. 2016 Lock-in in vortex-induced vibration. J. Fluid Mech. 794, 565–594.
- NITTI, A., DE CILLIS, G. & DE TULLIO, M.D. 2022 Cross-flow oscillations of a circular cylinder with mechanically coupled rotation. *J. Fluid Mech.* **943**, A30.
- PRANTL, L.1926 Application of the 'Magnus effect' to the wind propulsion of ships. NASA Tech. Rep. 367.
- PRASANTH, T.K. & MITTAL, S. 2008 Vortex-induced vibrations of a circular cylinder at low Reynolds numbers. *J. Fluid Mech.* **594**, 463–491.
- SARPKAYA, T. 2004 A critical review of the intrinsic nature of vortex-induced vibrations. *J. Fluids Struct.* **19**, 389–447.
- SINGH, S.P. & MITTAL, S. 2005 Vortex-induced oscillations at low Reynolds numbers: hysteresis and vortex-shedding modes. J. Fluids Struct. 20, 1085–1104.
- SOTI, A.K., THOMPSON, M.C., SHERIDAN, J. & BHARDWAJ, R. 2017 Harnessing electrical power from vortex-induced vibration of a circular cylinder. *J. Fluids Struct.* **70**, 360–373.
- SWANSON, W.M. 1961 The Magnus effect: a summary of investigations to date. *Trans. ASME J. Fluids Engng* 83, 461–470.
- TAHERI, E., ZHAO, M. & WU, H. 2023 The enhancement of flow induced vibration of a circular cylinder using a rotating control rod. *Phys. Fluids* **35**, 043607.

M. Zhao, Q. Zhang and Y. Liu

- VICENTE-LUDLAM, D., BARRERO-GIL, A. & VELAZQUEZ, A. 2018 Flow-induced vibration control of a circular cylinder using rotational oscillation feedback. *J. Fluid Mech.* **847**, 93–118.
- WILLIAMSON, C.H.K. & GOVARDHAN, R. 2004 Vortex-induced vibrations. *Annu. Rev. Fluid Mech.* 36, 413–455.
- YADAV, N. & BAREDAR, P. 2018 A review on piezoelectric energy harvesting system using vortex induced vibration. In *AIP Conference Proceedings*, vol. 2039, pp. 020054. AIP Publishing.
- ZHANG, X., CHEN, D., TANG, Y., LIN, Y., LIU, J. & PAN, G. 2024 Vortex-induced vibration and energy harvesting of cylinder system with nonlinear springs. *Phys. Fluids* **36**, 105189.
- ZHAO, M. 2013 Flow induced vibration of two rigidly coupled circular cylinders in tandem and side-by-side arrangements at a low Reynolds number of 150. *Phys. Fluids* **25**, 123601.
- ZHAO, M. 2020 Effects of natural frequency ratio on vortex-induced vibration of a circular cylinder in steady flow. Phys. Fluids 32, 073604.
- ZHAO, M. 2023 A review of recent studies on the control of vortex-induced vibration of circular cylinders. *Ocean Engng* **285**, 115389.
- ZHAO, M. & CHENG, L. 2011 Numerical simulation of two-degree-of-freedom vortex-induced vibration of a circular cylinder close to a plane boundary. *J. Fluids Struct.* 27, 1097–1110.
- ZHAO, M., CHENG, L., TENG, B. & DONG, G. 2007 Hydrodynamic forces on dual cylinders of different diameters in steady currents. *J. Fluids Struct.* 23, 59–83.